Solvent-Induced Self-Assembly of Polymer-Tethered Nanorods

Linli He,[†] Linxi Zhang,*,[‡] Yisheng Ye,[†] and Haojun Liang[§]

Department of Physics, Zhejiang University, Hangzhou 310027, P. R. China, Department of Physics, Wenzhou University, Wenzhou 325027, P. R. China, and Department of Polymer Science and Engineering, University of Science and Technology of China, Hefei, Anhui 230026, P. R. China

Self-assembly behaviors of polymer-tethered nanorods in the selective solvent are systematically investigated via a dissipative particle dynamics (DPD) simulation method. Three types of polymer-tethered nanorods are considered: one end tethered, both ends tethered, and middle tethered. The solvent-induced diverse morphologies and morphological transitions depend on the topology, rod/tether length ratio, solvent selectivity, and mixed solvent content. In the pure rod-selective solvent (solvent I) or the pure tether-selective solvent (solvent II), the ordered micellar structures include: cylinders, hexagonal cylinders, bilayer lamellae, lamellae/cylinder mixed phases, inverted hollow cylinders, and nematic bundles. These micelles are formed by the competition among the stretching of tethers, liquid crystalline of rods, interfacial energy, and solvent selectivity. In the I/II mixed solvent, with varying mixed solvent content in sequence (i.e., changing the solvent quality for the blocks), the reversible morphological transitions and fantastic intermediate phases (e.g., liquid crystalline phase) are observed, which correspond directly to the case of that induced by varying the rod/tether length ratio in the pure solvent. It is concluded that improving the selective solvent content is equivalent to increasing the soluble block ratio. The present study reveals that the morphology and morphological transition of polymer-tethered nanorods could be significantly manipulated through topology, block length, and solvent, especially the selectivity.

1. Introduction

Recent studies have been used to investigate the use of soft-matter tethers, such as flexible polymers, grafted to the surface of model nanoparticles, to facilitate the self-assembly of nanoparticles into ordered arrays.[1−3] This type of polymer-tethered nanoparticle constitutes a class of "shape amphiphiles"—geometric objects made of solvent-loving and solvent-hating parts.[4] A series of polymer-tethered nanoparticles can be constructed by grafting the flexible polymers with different numbers and grafted placements[5−7] to various architectural nanoparticles, such as nanospheres,[8] nanorods,[9] nanocubes,[10] nanoplates,[11] and nanoprisms.[12] Their self-assembled structures are far richer than those known for conventional block copolymer, surfactant, and liquid-crystal systems because of the nanoparticle geometry, the tether-grafted methods, and the immiscibility between nanoparticle and tether.

It is well-known that high-aspect-ratio nanoparticles, for example, nanorods (NRs), are different from spherical nanoparticles due to the effect of the additional orientational entropy resulting from the particles' anisotropy. Their nanometer-scale dimensions and shape anisotropy make them good candidates for wide applications, and they receive considerable attention.[13−17] Obviously, the polymer-tethered nanorod (PTN) is comprised of the rigid nanorod and flexible polymer chain. Conventional rod−coil-type block copolymers are the limit of PTN. Several common topologies of PTN have been synthesized experimentally, with a flexible polymer tethered to the end or the middle of the rod.[18−20] Three typical PTNs will be discussed in our

* Corresponding author. E-mail: lxzhang@zju.edu.cn.
† Zhejiang University.
‡ Wenzhou University.
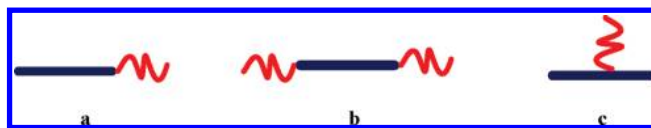§ University of Science and Technology of China.

Figure 1. Representative polymer-tethered nanorods. (a) One end tethered (PTN-1). (b) Both ends tethered (PTN-2). (c) Middle tethered (PTN-3).

following report: (a) one end tethered, (b) both ends tethered, (c) middle tethered (see Figure 1), corresponding to linear rod−coil, linear coil−rod−coil, and T-shaped rod−coil block copolymers. Briefly, for the conventional type coil−coil block copolymers, the driving forces for governing morphology formation and morphological transformation include the topology, block length, the interaction between blocks, concentration, temperature, and additives, etc. Compared to conventional block copolymers only composed of flexible blocks, the self-assembly of PTN-type copolymer molecules is no longer solely determined by the above factors, e.g., the phase separation between the blocks, but can also be affected by other processes, e.g., the aggregation of the rigid segments into liquid crystalline (LC) domains.[21] Moreover, they are able to form supramolecular architectures endowed with various functionalities through the rod blocks.[22−24] Rich morphologies arising from the self-assembly of PTN in the bulk have been observed experimentally,[25−27] theoretically,[28−30] and by simulations.[27,31,32] Experimentally, e.g., there are lamellar, perforated lamellar, 2D hexagonal columnar, 3D hexagonally perforated lamellar,[25] and 3D bicontinuous cubic structures[26] and filled cylindrical and hollow tubular scrolls.[27]

Besides their phase behaviors in the bulk, solvent-induced various peculiar and even supramolecular structures from the PTN solution also have been observed experimentally,[33−37] theoretically,[38] and by simulations.[39−42] For classical coil−coil

copolymer solutions, it tends to have rounded interfaces to minimize the interfacial contact between the solvent and the less soluble block. However, in coil-tethered rod copolymer systems, besides the phase separation between the blocks, packing of the rigid blocks at a curved interface creates liquid crystalline defects. Therefore, interfacial energy, liquid crystalline defect energy, coil stretching entropy, and packing constraints are critical to determine the nanostructures of PTN dissolved in solvent, especially the solvent selectivity. Recently, Lin et al. extended the lattice theory to describe the microphase separation behavior of a rod−coil diblock copolymer in a nonselective solvent. The rod−coil diblock copolymer exhibited lyotropic mesophases with lamellar, cylindrical, and spherical structures when the copolymer concentration was above a critical value.[38] Horsch et al. used molecular simulations to study the PTN in a coil-selective solvent. With different concentrations of PTN, they predicted the phases of a cubic phase, a smectic C phase, a tetragonally perforated lamellar phase, and a honeycomb phase.[39] Koh and Loos et al. experimentally investigated rod−coil block copolymers in solution. In a rod-selective solvent, they observed a number of different morphologies, including vesicles, spherical, cylindrical, and planar disklike micelles.[33,34] In contrast, they observed crew-cut micelles in a coil-selective solvent and star aggregates in a common solvent.[33]

Previous studies have reported the rich morphologies of PTN in solutions, mainly considering various factors such as the concentration and temperature,[39−41,43] polymer−solvent interactions,[38] and nanorod−nanorod interactions.[44] However, a general framework accounting for the self-assembly of PTN induced by different selective solvents and varied block characteristics is not available at the moment. Moreover, the investigation on the transition process from one phase to another phase is significant. Recently, there are a few experimental studies[45−50] about the effects of the mixed solvent on the self-assembled nanostructures of PTN. However, almost all experimental studies so far focus on this type of mixed solvent systems, where one solvent is selective for either segment (rod or tether), and the other is common. Tung et al. experimentally used two mixed solvent systems of THF/methanol (MeOH) and THF/ethyl acetate (EA) to probe the morphology change of PF-b-PTMSPMA, in which MeOH and EA are selective for rod and coil blocks respectively, while THF is the common solvent. Various morphologies of spheres, cylinders, large compound micelles, and hollow spherical micelles were observed by varying the solvent content.[48] Few related theoretical and simulation studies about the induction of mixed solvent on the PTN assemblies have been reported at present.

It is well predicted that the morphologies and morphological transitions of PTN may depend on the topology, rod/tether length ratio, solvent selectivity, and mixed solvent content. In this study, we extend the dissipative particle dynamics (DPD) method to investigate the self-assembled behaviors of three types of PTNs (one end, both ends, and middle tethered nanorods, shown in Figure 1) dissolved in pure solvent or mixed solvent with reverse selectivity. We first present the rich self-assembled morphologies with varied rod and tether length and then analyze the transition process from one phase to another phase. Finally, we deeply explore the induced morphological transition by continuously varying the content of two mixed solvents in comparison to the mixed solvent systems in experiments.[45−50]

2. Model and Simulation Method

The dissipative particle dynamics (DPD) technique[51] was originally introduced as a method of accessing larger length and time scales in computer simulations than conventional molecular dynamics. It has been successfully further developed to investigate the generic properties of macromolecular systems, e. g., the phase morphology and dynamics of a number of types of soft matter systems such as block copolymers,[52] polymer brushes,[53] and nanoparticle−polymer composites.[54,55]

Within the DPD approach,[51] a "beads" or DPD particle represents the center of mass of a group of atoms clustered together. The total force acting on a particular bead i is the sum of a conservative force, a dissipative force, and a random force

$$\vec{f}_i = \sum_{i \neq j} (\overrightarrow{F}_{ij}^{C} + \overrightarrow{F}_{ij}^{D} + \overrightarrow{F}_{ij}^{R}) \tag{1}$$

$$\overrightarrow{F}_{ij}^{C} = a_{ij}\omega(r_{ij})\hat{r}_{ij} \tag{2}$$

$$\overrightarrow{F}_{ij}^{D} = -\gamma\omega^2(r_{ij})(\hat{r}_{ij}\cdot\vec{v}_{ij})\hat{r}_{ij} \tag{3}$$

$$\overrightarrow{F}_{ij}^{R} = \sigma\omega(r_{ij})\theta_{ij}\hat{r}_{ij} \tag{4}$$

The conservative force $\overrightarrow{F}_{ij}^{C}$ is the soft repulsion acting along the intermolecular vector, where a_{ij} is a maximum repulsion between beads i and j; and $\vec{r}_{ij} = \vec{r}_i - \vec{r}_j$, $r_{ij} = |\vec{r}_{ij}|$, $\hat{r}_{ij} = \vec{r}_{ij}/r_{ij}$. For the weight function $\omega(r)$, we adopt the commonly used form

$$\omega(r) = \begin{cases} 1 - r/r_c & r_{ij} < r_c \\ 0 & r_{ij} \geq r_c \end{cases} \tag{5}$$

which is an r-dependent weight function vanishing for $r_{ij} \geq r_c$, where r_c is the cutoff radius. The other two forces ($\overrightarrow{F}_{ij}^{D}$ and $\overrightarrow{F}_{ij}^{R}$) act as a heat sink and a heat source, respectively, which effectively combine to thermostat the system, where $\vec{v}_{ij} = \vec{v}_i - \vec{v}_j$ and θ_{ij} is a randomly fluctuating variable with Gaussian statistics: $\langle\theta_{ij}(t)\rangle = 0$ and $\langle\theta_{ij}(t)\theta_{kl}(t')\rangle = (\delta_{ik}\delta_{jl} + \delta_{il}\delta_{jk})\delta(t - t')$. Also, there is a relation between the friction coefficient γ and the noise amplitude σ as follows

$$\sigma^2 = 2\gamma k_B T \tag{6}$$

where k_B is Boltzmann's constant. In our simulation, $\gamma = 6.57$ and the temperature $k_B T = 1$. Therefore, $\sigma = 3.62$ according to eq 6. In DPD, it is convenient to use reduced units.[52] The unit of length is defined by the cutoff radius r_c; the unit of mass is defined by the mass m of the particles (which is chosen to be the same for all the particles); and the unit of energy is defined by $k_B T$.

The important physical feature of the PTN molecule is the rigidity of the nanorod. According to the approach taken by previous studies[55,56] in the DPD simulation, the rigid nanorod can be constructed by a number of DPD beads L_r, with a fixed small distance D_{b-b} between consecutive beads. Naturally, the real length of a nanorod can be calculated by $L_{nr} = (L_r - 1) \times D_{b-b}$. To readily compare with the tether length, we use the DPD bead number L_r in a nanorod to characterize the rod length. In our study, D_{b-b} is fixed at 0.3, and L_r ranges from 2 to 16; i.e., L_{nr} ranges from 0.3 to 4.5. Then, the tethered polymer

Solvent-Induced Self-Assembly of PTNs

J. Phys. Chem. B, Vol. 114, No. 21, 2010 **7191**

consisting of L_t DPD beads is connected by the spring force $\vec{f}_i^S$, which acts between the connected beads in a chain and has the form of

$$\vec{f}_i^S = \sum_j C\vec{r}_{ij} \qquad (7)$$

where C is a harmonic type spring constant for the connecting pairs of beads in a polymer chain, which is chosen to be equal to 4 here. Additionally, the solvent molecules are also represented by individual DPD beads. Totally, there are three types of DPD beads in our system: rod (r), tether (t), and solvent (s). The Newton equations for all particles' positions and velocities are integrated by a modified version of the velocity Verlet algorithm[52] with the step size of $\Delta t = 0.04\tau$, where τ is the natural unit of time defined as $r_c(m/k_BT)^{1/2}$. Full details are given in our previous report.[55]

The simulations are performed in a cubic box of constant volume $V = L \times L \times L$. Periodic boundary conditions are applied in all three directions. Finite size effects need to be considered and avoided. Here, we have investigated three simulated systems with different sizes of $9 \times 9 \times 9$, $11 \times 11 \times 11$, and $13 \times 13 \times 13$ DPD units, which present the same results. For easy comparison, we focus on the $13 \times 13 \times 13$ DPD units system, containing 10 985 DPD beads for the density of $\rho = 5$. Here, the number of PTN molecules is fixed at 350, and the total number of DPD beads (PTN + solvent) in the simulation box is chosen to fix the overall reduced density of the simulation box, so the number of solvent beads is varied according to the reduced density ρ.

It was found that the repulsion parameter a_{ij} in eq 2 can be chosen according to[52]

$$a_{ii}\rho = 75k_BT \qquad (8)$$

$$a_{ij} \approx a_{ii} + 3.27\chi_{ij} \; (\rho = 3) \qquad (9)$$

$$a_{ij} \approx a_{ii} + 1.45\chi_{ij} \; (\rho = 5) \qquad (10)$$

where a_{ii} is the repulsion parameter between particles of the same type. We have used the density of $\rho = 5$, hence the repulsion parameter $a_{ii} = 15k_BT$, and a_{ij} is obtained according to eqs 8 and 10, where the correspondence between our repulsion parameters a_{ij} and the Flory−Huggins parameters χ places our results in the proper context. Correspondingly, the values of a_{ij} between the three types of DPD beads (r, t, and s), are given by $a_{rr} = a_{tt} = a_{ss} = 15$ and $a_{rt} = 45$. At the same time, a_{rs} and a_{ts} change according to the solvent selectivity. Here, we investigate the self-assembly of PTN under different solvent conditions. The solvent I is a rod-selective solvent (i.e., good for rods and poor for tethers with $a_{rs} = 15$ and $a_{ts} = 45$), while the solvent II is a tether-selective solvent (i.e., poor for rods and good for tethers with $a_{rs} = 45$ and $a_{ts} = 15$), having the reverse selectivity in contrast to solvent I.

Every obtained morphology is calculated after long iteration steps until the system completely reaches equilibrium states and the stable structure is not changed with time. As shown in Figure 2a, with the increase of the iteration step, the total energy ε of the system decreases rapidly and reaches equilibrium. The insets indicate the structure has been basically stable after 1.3×10^5 steps. Here, at least 2.0×10^5 steps are performed to ensure the acquirement of every equilibrium structure. Meanwhile, it
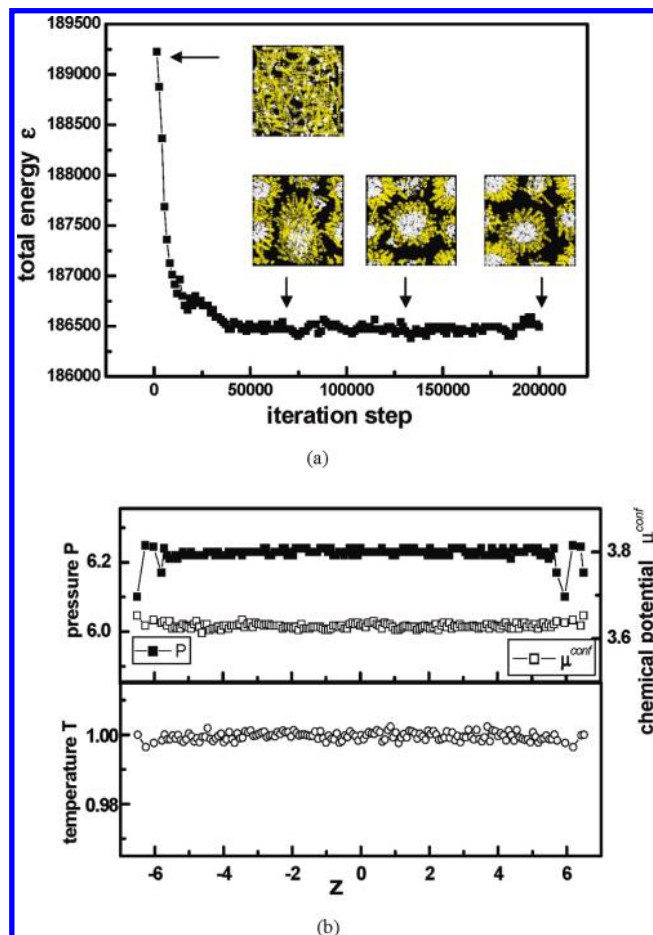

Figure 2. Thermodynamic equilibrium for the simulated system. (a) The total energy of the system as a function of the iteration step. The insets represent the morphologies of the system at the iteration steps of 0, 0.7×10^5, 1.3×10^5, and 2.0×10^5, respectively. (b) The profiles of local temperature T, pressure P, and configurational chemical potential μ^{conf} for the system at the iteration step of 2.0×10^5 along the z-axis direction, respectively.

is necessary to check the thermodynamic consistency for every obtained system. The calculation of local temperature T, pressure P,[57,58] and configurational chemical potential μ^{conf}[58−60] along a specific direction is useful to check the thermal, mechanical, and chemical equilibrium inside the simulation cell because these parameters must be constant through the system. Because the local density varies across the simulation cell, we calculate the configurational chemical potential μ^{conf} by the test particle insertion method,[59] considering the interaction energy of a test particle inserted in the box, which can be used to validate the local chemical equilibrium.[58,60] The expression of the calculated chemical potential $\mu^{conf}(z)$ as a function of z is as follows[58,60]

$$\mu^{conf}(z) = k_BT \ln\left[\frac{<\rho(z)>}{<\exp\left(-\dfrac{\Delta U}{k_BT}\right)>}\right] \qquad (11)$$

Here, $\rho(z)$ is the number density; ΔU is the interaction energy of the test particle at height z with the other particles in the box; and $<...>$ denotes the ensemble average. Figure 2b shows that the profiles of the local pressure P and configurational chemical potential μ^{conf} (upper part) and the local pressure T (lower part) are also independent of z, indicating the thermodynamic equilibrium and consistency of the system.
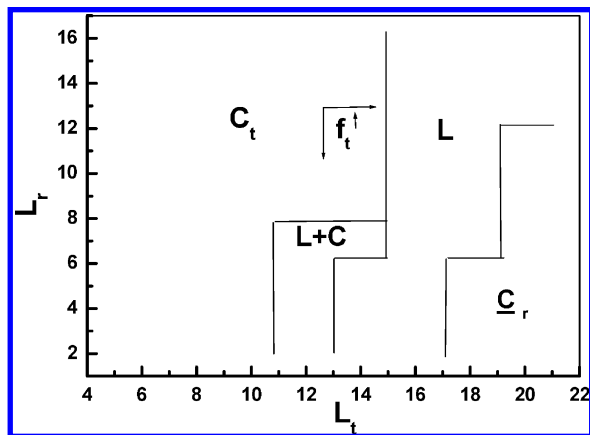
Figure 3. L_r vs L_t morphological phase diagram of PTN-1 dissolved in the rod-selective solvent (solvent I). The lines represent the estimated phase boundaries as visual guides to identify the regions in which specific ordered structures are observed. C_t, $L + C$, L, and C_r correspond to tether filled cylinders, lamellae/cylinder mixed phases, bilayer lamellae, and rod-formed hollow cylinders, respectively.

3. Results and Discussion

In this study, we focus on three types of PTN molecules as shown in Figure 1: (a) one end tethered (PTN-1), (b) both ends tethered (PTN-2), and (c) middle tethered (PTN-3). To illustrate the influence of solvent selectivity on the assembled structures, we investigate three cases for the above PTN dissolved in: (1) the pure solvent I, (2) the pure solvent II, and (3) the I/II mixed solvent, respectively. Meanwhile, under the pure solvent conditions, we also predict the role of block (rod/tether) length on the assembled structures.

3.1. One End Tethered Nanorods (PTN-1). 3.1.1. In the Rod-Selective Solvent (Solvent I). For PTN-1 dissolved in solvent I, which is a rod-selective solvent, the phase diagram of rod length L_r versus tether length L_t is presented in Figure 3. We observe four distinct micellar structures: C_t, $L + C$, L, and C_r. The details of these phases are discussed in the following. The lines in Figure 3 represent the estimated phase boundaries as visual guides to identify the regions in which specific ordered structures are observed.

Figure 4 presents some typical snapshots, rod concentration, and density profiles for the case of PTN-1 dissolved in solvent I, where diverse micelle morphologies are observed: tether filled cylinders (C_t), lamellae/cylinder mixed phases ($L + C$), bilayer lamellae (L), and rod-aggregated hollow cylinders (C_r). For example, when $L_r = 7$, a cylinder structure is observed at a short tether with $L_t = 6$ as shown in Figure 4a1, which consists of the dissoluble tether core and the soluble rod corona. The repulsion of the coil tether block from the solvent mainly promotes the formation of highly curved cylindrical micelles (C_t). Generally, these rounded interfaces can minimize the interfacial contact between the dissoluble tether and solvent. As tether length L_t is increased to 16, we observe a lamellae (L) composed of a bilayer, in which the dissoluble tethers are located in the middle of the lamellae and the soluble rods are directed toward the solvent as shown in Figure 4c1. These results are similar to the experimental studies for thiophene-containing rod−coil block copolymers in solution.[62] In addition, a coexisting mixed structure ($L + C$) of lamellae and cylinder is found in the process of transformation from the cylindrical to lamellar phase, as shown in Figure 4b1. The morphological transition from a cylindrical (C_t) to lamellar membrane (L) is because the swelling of the inner tether core is enhanced with increasing tether length L_t, leading to an increased interfacial area for

lamellae formation. The bilayer lamellae structure can accommodate the desire of the larger tether blocks to occupy more interfacial area and simultaneously reduce the liquid crystalline penalty for rod packing at the curved interface. Upon further increase of tether length to $L_t = 20$, an inverted morphology of a rod-aggregated hollow cylinder (C_r) is observed in Figure 4d1, where the solvents are repelled to be localized at the inner of the hollow cylinder, and rods are packed radially and side by side. The further swelling of the middle domain of the lamellae is caused by the increase of dissoluble block length L_t. Hence, the formation of the hollow cylinder (C_r) is an efficient way to minimize total surface energies and to relax flexible chain stretching. Similar hollow spherical micelles are also observed experimentally in aggregates of rod−coil block copolymers in mixed solvent.[47] In Figures 4a2−d2 and a3−d3, the rod block concentration and density profiles, corresponding to the morphologies in Figure 4a1−d1, can further embody and characterize the different phases. The above phase transition horizontally corresponds to the phase diagram in Figure 3, with a fixed rod length $L_r = 7$ and the increased tether lengths L_t. Vertically, for a fixed tether length $L_t = 14$ with the decreased rod lengths $L_r = 9, 7, 5,$ and 3, the similar morphological transitions from cylindrical (C_t) to lamellar/cylindrical mixed structure ($L + C$) and to bilayer lamellae (L) are clearly shown in Figure 4a4−d4. Meanwhile, the corresponding rod concentration and density profiles are presented in Figures 4a5−d5 and 4a6−d6. Whether the tether length L_t is increased from $L_t = 6$ to $L_t = 20$ with $L_r = 7$ in Figure 4a1−d1 or the rod length L_r is decreased from $L_r = 9$ to $L_r = 3$ with $L_t = 14$ in Figure 4a4−d4, it can come down to the increase of the tether block ratio f_t ($\equiv L_t/(L_r + L_t)$). For example, in Figure 4a1−d1, the tether block ratio f_t is increased from $f_t = [6/(6 + 7)] = 46\%$ to $f_t = [20/(20 + 7)] = 74\%$, while in Figure 4a4−d4 it is increased from $f_t = [14/(14 + 9)] = 61\%$ to $f_t = [14/(14 + 3)] = 82\%$. Both cases display the same morphological transition from cylindrical to lamellar phase. Hence, it indicates that the increase of f_t leads to an approximate tendency of morphological transition from the cylindrical to the lamellar phase even to inverted cylinder, to have a minimizing energy and better protect the tethers from unfavorable contact with solvent molecules.

In addition, we quantitatively analyze the above morphological transition from cylindrical (C_t) to lamellar membrane (L), through calculating the interfacial tension of the systems. The profile of interfacial tension σ along the interface orientation is calculated using the Irving−Kirkwood method[57,61]

$$\sigma = L\left[\langle p_{zz}\rangle - \frac{1}{2}(\langle p_{xx}\rangle + \langle p_{yy}\rangle)\right] \quad (12)$$

where $\langle ... \rangle$ denotes the ensemble average, and the component of the pressure tensor P_{xx} is obtained from the conservative

$$P_{xx} = \frac{1}{V}\left\langle \sum_i^{N_p} m_i v_{ix} v_{ix} + \sum_i^{N_p} \sum_{j>i}^{N_p} F_{ijx} x_{ij}\right\rangle \quad (13)$$

where N_p is the number of all DPD particles; $x_{ij} = x_i - x_j$; and F_{ijx} are the position and force components in the x-axis direction between particles i and j. The components P_{yy} and P_{zz} are obtained by replacing x with y and z in eq 13. Figure 5 shows the interfacial tension σ profiles versus the tether length L_t for three cases of the fixed rod length $L_r = 5, 7,$ and 9, where the black, red, green, and blue in the curves represent the morphol-
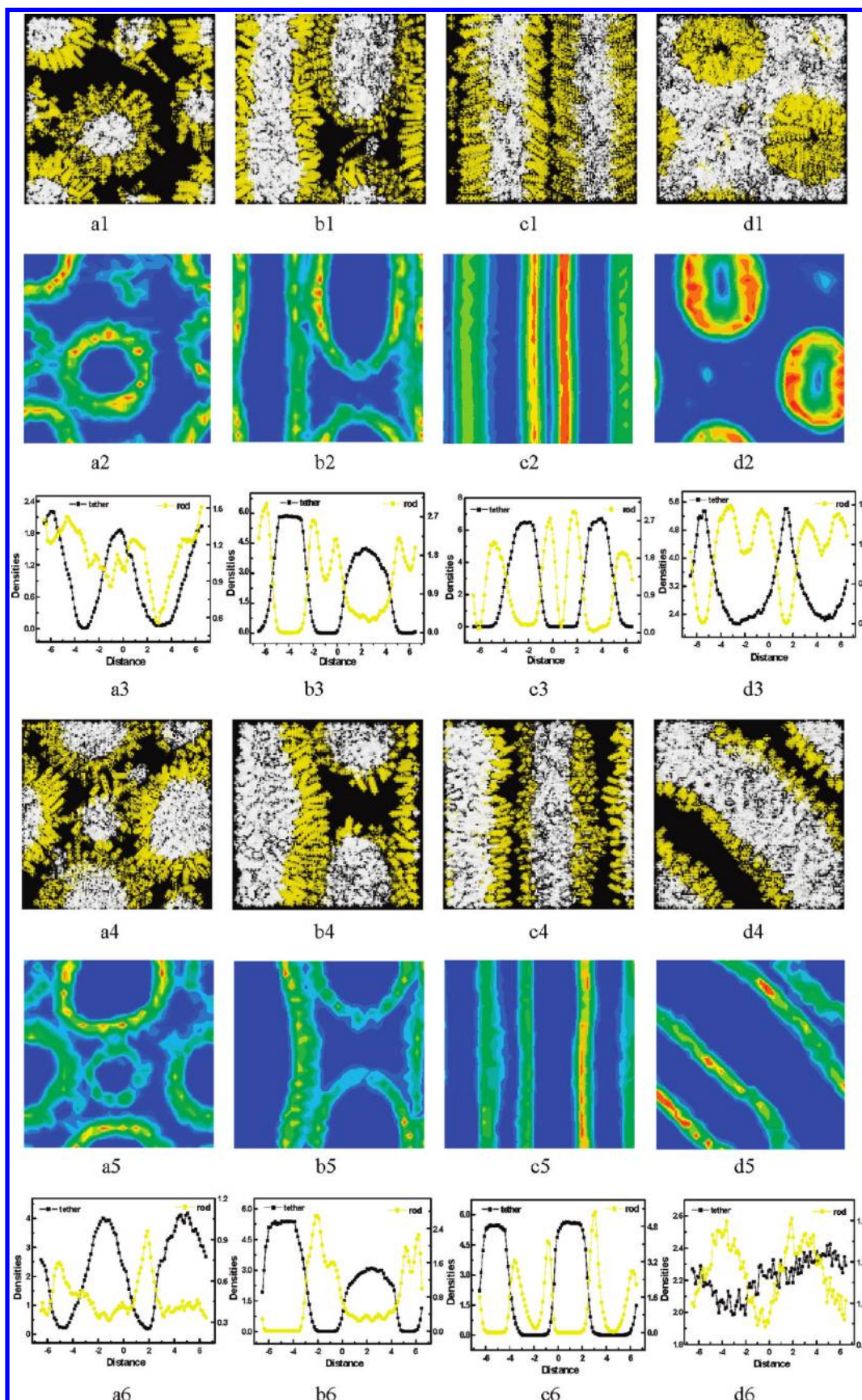
Solvent-Induced Self-Assembly of PTNs

J. Phys. Chem. B, Vol. 114, No. 21, 2010 **7193**

Figure 4. Snapshots, rod concentration, and densities for systems of PTN-1 dissolved in the rod-selective solvent. In (a1−d1) to (a3−d3), $L_r = 7$ with L_t = 6, 12, 16, and 20. In (a4−d4) to (a6−d6), $L_t = 14$ with L_r = 9, 7, 5, and 3, respectively. The solvent has been removed for clarity. Rods are always presented in yellow. Tethers are presented PTN in white in morphologies and in black in density profiles, respectively.

ogies of C_t, $L + C$, L, and $\underline{C}_r$ (see Figure 3). Take the curve (line + dots) of $L_r = 7$. For example, when the tether length L_t

is increased, the interfacial tension σ gradually increases with, respectively, experiencing the coexisting phase ($L + C$) and
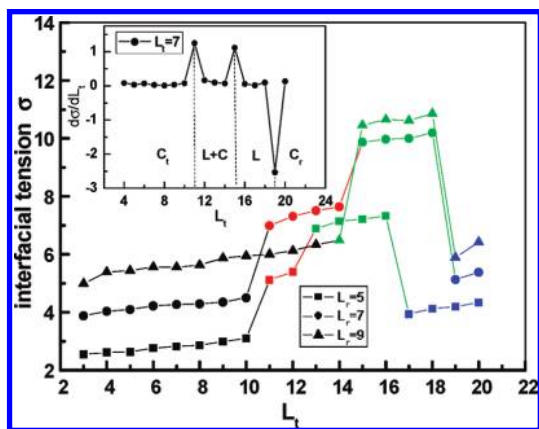
Figure 5. Interfacial tension σ as a function of L_t for $L_r = 5$, 7, and 9, respectively. The colors of black, red, green, and blue correspond to the morphologies of C_t, $L + C$, L, and $\underline{C}_r$. The inset represents the change rate ($d\sigma/dL_t$) of the interfacial tension σ versus L_t.

Figure 6. L_r vs L_t morphological phase diagram of PTN-1 dissolved in the tether-selective solvent (solvent II). B, C_r, and M correspond to nematic bundles, cylinders, and nonuniform size small micelles, respectively.

lamellar structure (L) and then decreases for the hollow cylinders ($\underline{C}_r$). The insets in the top left corner show the ratio $d\sigma/dL_t$ as a function of L_t for the $L_r = 7$ case, where the corresponding phases of C_t, $L + C$, L, and $\underline{C}_r$ are marked out and the peaks are located at $L_t = 11$, 15, and 19, corresponding exactly to the morphological transition points of the phase diagram shown in Figure 3. It is meaningful to explore the change rate ($d\sigma/dL_t$) of the interfacial tension σ versus L_t, and its curve peaks mark the phase transition points, just as liquid−solid-like and/or polymorphic transitions are often characterized by the heat capacity C_v as a function of temperature T ($C_v \equiv (dE)/(dT)$, and E is the internal energy).[63] It is clear that with the increase of tether length L_t and the swelling of the inner tether domains, the interfacial intension between the tether and rod block is required to be increased, which leads to an increased interfacial area and reduced interfacial curvature. The structures with less curvature can form as indicated by the transition from cylinder (C_t) to the coexisting structure ($L + C$) and then to the lamellar membrane (L) with no curvature. Finally, the σ decrease for the hollow cylinder ($\underline{C}_r$) is due to the relaxation of tether chain stretching.

3.1.2. In the Tether-Selective Solvent (Solvent II). Opposite to the case of solvent I, the PTN-1 dissolved in tether-selective solvent (solvent II) will form the unique self-assembled structures with the rod blocks at the core of the micelles. The morphological phase diagram of L_r versus L_t is presented in Figure 6. Three micellar morphologies, B, C_r, and M, are divided depending on the rod block ratio f_r ($\equiv L_r/(L_r + L_t)$). We will discuss these phases combining with the phase diagram in detail.

Vertically, the system snapshots for a fixed $L_t = 6$ with $L_r = 5$, 7, 9, and 11 (i.e., the value of f_r increases) are shown in Figure 7a1−d1. The morphological transition from cylinders (C_r) to nematic bundles (B) is clearly observed. In addition, Figure 7a1−c1 indicates that the core size of the cylinders in these structures becomes slightly large as the rod length L_r increases. Horizontally, also along with the f_r increasing case for a fixed $L_r = 5$ with decreased $L_t = 10$, 8, 6, and 2, the system snapshots are shown in Figure 7a2−d2. Several types of rod alignment within aggregated micelles are induced by varying the tether length L_t. At a long tether with $L_t = 10$, some small micelles (M) with different sizes are observed in Figure 7a1. As L_t is decreased to 8 and 6, the cylindrical micelles (C_r) are observed in Figure 7b2−c2, in which the rods order radially as the core. Finally, at a shorter tether with $L_t = 2$, the rods are aligned side by side to form the nematic bundles (B) shown in Figure
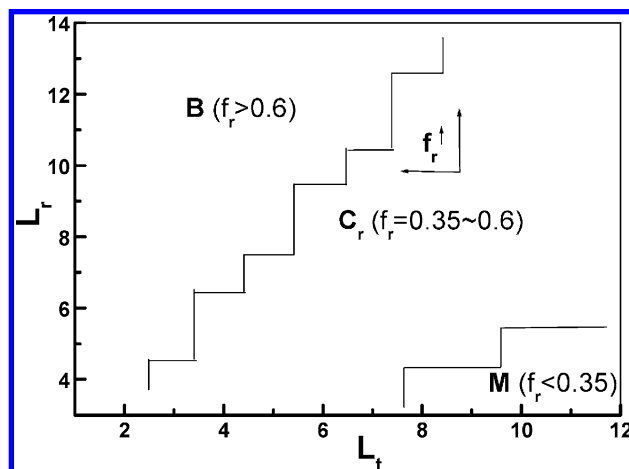
7d2. Combined with the phase diagram in Figure 6, we can conclude that if the rod block ratio f_r has a high value ($f_r > 0.6$, i.e., the rod length L_r is much larger than the tether length L_t), the rods favor parallel packing as bundles to minimize the interfacial energy between the rod blocks and solvent, and meanwhile the tether chains are too short to change the rod alignment. As the tether chain with a size comparable to the length of rod blocks ($f_r < 0.6$), the cylindrical aggregates are favored in the latter case, in comparison with the nematic bundle. The above morphology transition suggests the significance of the soluble tether length on the alignment of dissoluble rods and self-assembled structures of the PTN-1 block copolymers. The entropy loss as a result of the stretching of tethers increases with increasing tether length, and thus it prefers the cylindrical aggregates for reducing the tether stretching. Combined with the two cases of the varied L_r and L_t in Figures 7a1−d1 and 7a2−d2, it is equivalent to the increase of rod ratio f_r. It indicates that the shape and size of the aggregates of PTN-1 dissolved in solvent II are determined primarily by the relative rod ratio f_r.

3.1.3. In the I/II Mixture Solvent. For the I/II mixture solvent, we focus on a specific PTN-1 with $L_r = 7$ and $L_t = 6$. Figure 8a−e shows the morphologies of selected PTN-1 with the solvent II contents of 0, 30, 40, 70, and 100 vol %, respectively, in which 0 and 100 vol % correspond to the pure solvent I and II, and the tether filled cylinder (C_t) and rod filled cylinder (C_r) have been shown in Figure 4a1 and Figure 7b1 mentioned above. When the solvent II content increases from 0 to 30 and 40 vol %, the tether-selective solvent II penetrates into the tether core of the micelles, leading to enhanced degree of swelling of the tether core. The interfacial tension between the tether core and the rod corona is increased to require reducing the interfacial curvature. Thus, the micelle shape changes from cylinder (C_t) to bilayer lamellae (L) observed in Figure 8a−c. A clearer snapshot for the bilayer nematic lamellae is emphasized in Figure 8f. The similar morphological transitions from cylinder (C_t) to bilayer lamellae (L) have been presented in Figure 3 (along with the f_t increasing direction marked out by the arrows). It indicates that for the case of mixed solvent the partial increasing of the tether-selective solvent (solvent II) content is equivalent to enhancing the tether block ratio f_t of PTN-1 in the pure solvent I. Further increasing the solvent II content to 70 and 100 vol %, a backward analysis on this substitution process is more understandable. Contrarily, when the content of rod-selective solvent I replacing the tether-selective solvent II ranges from 0 (Figure 8e) to 30 vol % (Figure
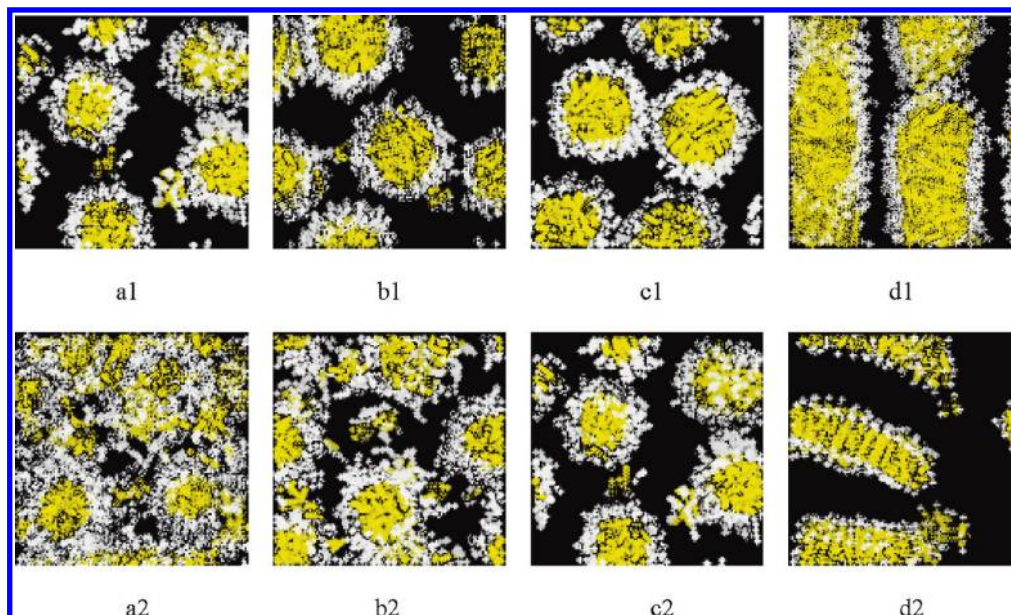
Figure 7. Simulation snapshots obtained from a system of PTN-1 dissolved in the tether-selective solvent. In (a1−d1), $L_t = 6$ with $L_r = 5, 7, 9,$ and 11. In (a2−d2), $L_r = 5$ with $L_t = 10, 8, 6,$ and 2, respectively.
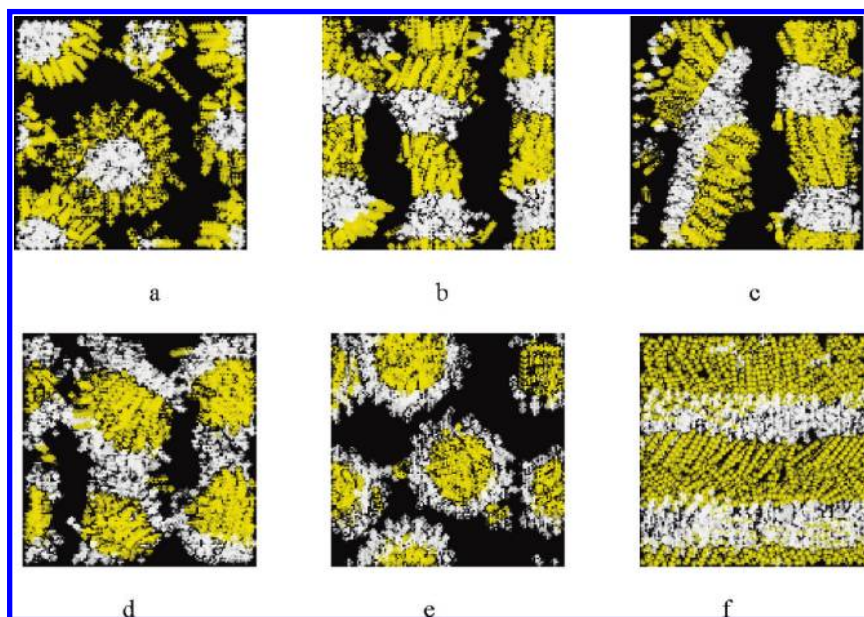

Figure 8. Morphological changes of PTN-1 in the I/II mixed solvents with the II contents of: (a) 0 vol %, (b) 30 vol %, (c) 40 vol %, (d) 70 vol %, and (e) 100 vol %. Here, $L_r = 7$ and $L_t = 6$. The lower image in (f) is the face view of the upper image in (b), which corresponds to the side view. The bead models of nanorods are presented in (f) for visualization.

8d), a micelle transition from inverted rod filled cylinders (C_r) to nematic bundles (B) is observed, which is also consistent with the morphological transitions presented in Figure 6 (along with the f_r increasing direction marked out by the arrows). Likewise, it also exhibits that the partial increase of the rod-selective solvent (solvent I) content is equivalent to enhancing the rod block ratio f_r of PTN-1 in a pure solvent II. The above micellar structures (C_t, L, B, and C_r) could be reversibly interchanged by varying the ratio of solvent I to II. Generally, in a mixed solvent with inverse selectivity, partially varying solvent quality for the block can induce a reversible morphological transition, which is equivalent to changing the corresponding block length ratio in a pure solvent case.

3.2. Two Ends Tethered Nanorods (PTN-2). *3.2.1. In the Rod-Selective Solvent (Solvent I).* Compared to the PTN-1 only tethered by one end, the symmetry from both tethered ends has

a significant influence on the self-assembly of PTN-2 block copolymers in solution. Meanwhile, the PTN-2 assemblies are more sensitive to the tether length. Once tether length is slightly long, the ordered phase will not be observed.

The PTN-2 are dissolved in solvent I, which is the rod-selective solvent. Totally, lamellae structures are observed from the side views in Figure 9a2−d2. For clarification, we just present the one lamellae of Figure 9a2−d2 in Figure 9a1−d1. When tether length is short, such as $L_t = 1$ or 2, the netlike lamellae are observed as shown in Figure 9a1−c1. The association of PTN-2 molecules in lamellae results from the aggregate of the tethers, liquid-crystal behavior of the rods, and the special structure from the rods tethered symmetrically. When tether length is increased, such as $L_t = 4$ (see Figure 9d1−d2), the swelling tethers aggregate into the middle of the lamellae and the rods with a planar orientation wrap the lamellae surface, to sufficiently protect the tether blocks from
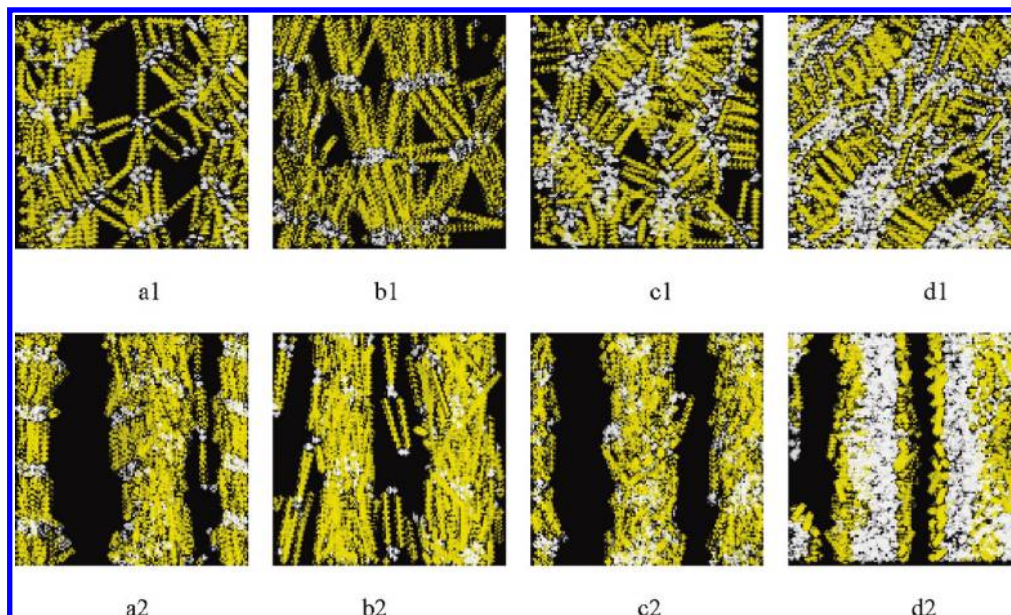
Figure 9. Simulation snapshots obtained from a system of PTN-2 dissolved in the rod-selective solvent. In (a1−b1), $L_t = 1$ with $L_r = 7$ and 11. In (c1−d1), $L_r = 7$ with $L_t = 2$ and 4. The upper images in (a1)−(d1) are the face views for a single lamellae. The lower images in (a2−d2) are the side views of the whole system.
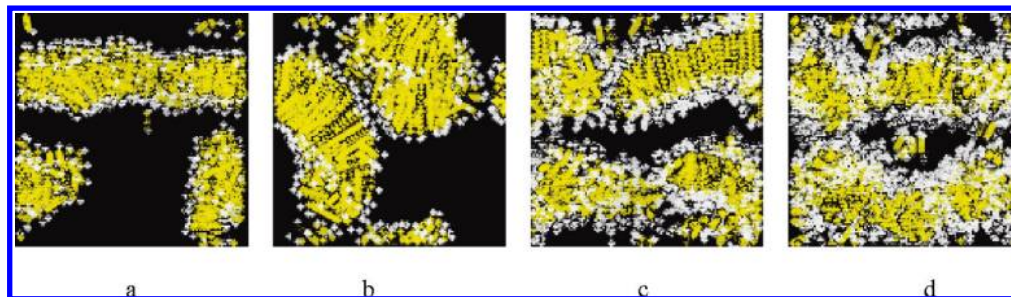

Figure 10. Simulation snapshots obtained from a system of PTN-2 dissolved in the tether-selective solvent. In (a−b), $L_t = 1$ with $L_r = 7$ and 11. In (c−d), $L_r = 7$ with $L_t = 2$ and 4.

unfavorable contact with solvent molecules. Moreover, the planar orientation of the rod is also energetically favored because they can order into a liquid crystalline (LC) state as postulated in experimental research.[34]

3.2.2. In the Tether-Selective Solvent (Solvent II). The PTN-2 is dissolved in solvent II, which is a tether-selective solvent. Totally, the bundles micelles (*B*) are observed in Figure 10a−d, similar to the observed structures for PTN-1 assemblies in solvent II mentioned above (see Figure 7d1−d2). The hydrophobic rod packs side by side as the core of the micelles and the hydrophilic tether consists of the corona. If tether length is slightly long, the side by side parallel alignment of a rod in bundles will be frustrated because of stretching energies of the tethers, such as $L_t = 4$ with $L_r = 7$ shown in Figure 10d. Likewise, the ordered phase can not be observed for any relatively long tether chain. Consequently, the self-assembly of PTN-2 in pure selective solvent I or II is dominated by the two difference processes: the association governed by tethers in the former and the micellization governed by rods in the latter; however, the effects of liquid crystalline behavior of rods are always maintained in both cases.

3.2.3. In the I/II Mixture Solvent. For the I/II mixture solvent, we focus on a specific PTN-2 with $L_t = 1$ and $L_r = 7$. Figure 11 shows the morphologies of the selected PTN-2 with the solvent II contents of 0, 20, 30, 40, and 100 vol %, respectively, where 0 and 100 vol % correspond to the two cases of the pure solvent I and II (see Figure 9a1 and Figure

10a). Whether the rod-selective solvent (solvent I) is replaced by tether-selective solvent (solvent II) or conversely replaced, a well smectic LC phase is observed in sequence by varying solvent content, as shown in Figure 11c. A clearer side view for the LC lamellar phase is emphasized in Figure 11f. Upon the mixed solvent I/II, the PTN-2 molecules simultaneously underwent four difference processes: the formation of associate, the formation of micelles, the breakdown of associate, and the breakdown of micelles, always with the LC phase behavior from rods. Once the competition between the association governed by tethers and the micellization governed by rods reaches equilibrium at some mixed solvent content, the LC behavior of rods will dominate the final morphologies of the PTN-2 assembles, as shown in Figure 11c,f.

3.3. Middle Tethered Nanorods (PTN-3). ***3.3.1. In the Rod-Selective Solvent (Solvent I).*** Comparatively, we also demonstrate the results that a tether attaches to the middle position of a nanorod and gives rise to novel structures, which are significantly different from those observed for the end-tethered nanorod. For the solvent I, the morphological phase diagram of L_r versus L_t is presented in Figure 12. It demonstrates that the self-assembled structure of PTN-3 also depends on rod and tether lengths. We observe three distinct phases: I, HC_t, and L. The specific morphologies, rod concentration profiles, and tether removed snapshots of PTN-3 assemblies dissolved in solvent I are presented in Figures 13a1−c1, a2-c2, and a3-

Solvent-Induced Self-Assembly of PTNs

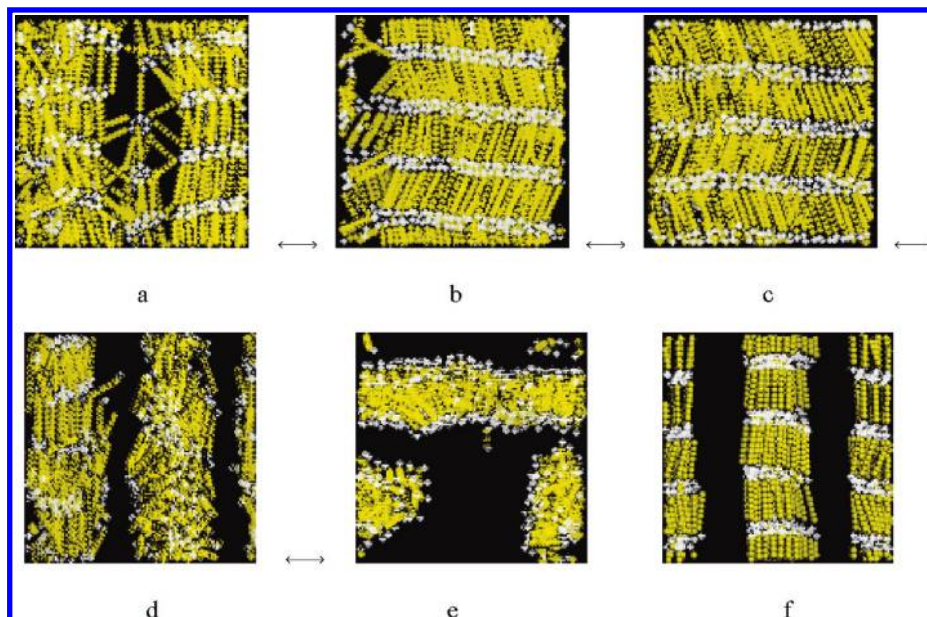*J. Phys. Chem. B, Vol. 114, No. 21, 2010* **7197**

Figure 11. Morphological changes of PTN-2 in the I/II mixed solvents with the II contents of: (a) 0 vol %, (b) 20 vol %, (c) 30 vol %, (d) 40 vol %, and (e) 100 vol %. Here, $L_t = 1$ and $L_r = 7$. The lower image in (f) is the side view of the smectic LC phase, whose face view is shown in (c).
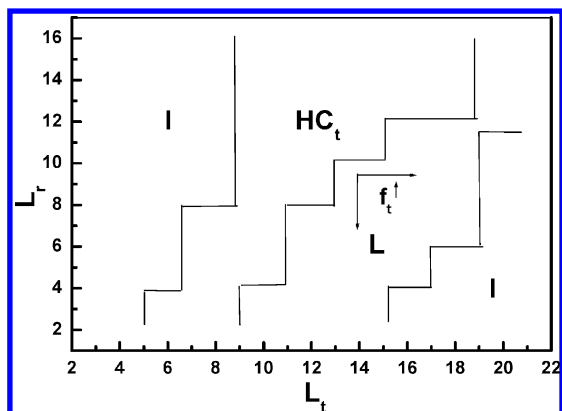

Figure 12. L_r vs L_t morphological phase diagram of PTN-3 dissolved in the rod-selective solvent. I, HC_t, and L correspond to isotropic phases, tether-filled hexagonal cylinders, and stepped bilayer lamellae, respectively.

c3. For a short rod with $L_r = 3$, the weak desire for the rods to align and maximized stretching of tethers lead to the formation of the isotropic phase (I), as shown in Figure 13a1−a3. As rod length L_r is increased to 9, the PTN-3 molecules self-assemble into a stepped bilayer lamellae (L) with alternating bilayers of rods and tethers, in which the rods are aligned parallel to each other with rod tilt to the layer planes, as shown in Figure 13b1−b3. A face view for the local packing of the rods in a single layer is emphasized in Figure 13a4. The emergence of the bilayer structure is a result of the competition between maximizing the rod−rod contacts and the entropy contributed by the tethers. A similar rectangular stepped ribbon phase has been predicted by Horsch et al.[41] Upon further increase of $L_t = 11$, a filled hexagonal cylinder (HC_t) is observed in Figure 13c1−c3. The hydrophobic tethers aggregate into the cores, and the packed rod blocks wrap tangentially[34] the surface of the aggregated tether core to form an outer layer. The rods are organized approximately parallel to each other with a rod tilt angle with respect to the cylindrical axis, as shown in Figure 13b4. Therefore, vertically corresponding to the phase diagram (see Figure 12), with the increase of rod length L_r, i.e., the value of f_t decreases, and the ordered morphologies are transformed

from the isotropic phase (I) to the stepped bilayer lamellae (L) to the hexagonal cylinder (HC_t). It suggests that the increase of rod length L_r endows the rods with the ability to minimize energy and maximally protect the tethers from unfavorable contact with solvent molecules.

3.3.2. In the Tether-Selective Solvent (Solvent II). Surprisingly, when the PTN-3 is dissolved in solvent II, the system exhibits a concentric cylinder phase, which is the only ordered phase observed and exists in the very limited range of rod and tether length. As shown in Figure 13d1−d3, the cylinder has a hierarchical structure comprised of three parts: the core of aggregated tethers, the sublayer of rod bilayers, and the outer layer of tethers. The structures are similar to the scroll structures observed experimentally in the bulk of rod−coil copolymers.[27] Likewise, the rods packed as a bilayer within the sublayer wrap tangentially the surface of the tether core. From Figure 13b4 and c4, the local packing of the rods in a single layer indicates that the rods in a concentric cylinder have a packing structure essentially identical to hexagonal cylinder (HC_t). Whether in a hexagonal cylinder or in a concentric cylinder, a chiral arrangement of rods packed as the layer is preferred due to the competition between the interfacial energy and the elastic stretching energy of the flexible tethers, which is also explored from experimental studies.[27] For middle tethered nanorods (PTN-3), the peculiar crystalline ordering of the rods in layers is favored over other arrangements because both the rod contacts and the free volume of the tethers are maximized, as a result of its special structure from middle grafted placement.

3.3.3. In the I/II Mixture Solvent. For the I/II mixture solvent, we focus on a specific PTN-3 with $L_t = 14$ and $L_r = 11$. Figure 14 shows the morphologies of selected PTN-3 with the solvent II contents of 0, 30, and 100 vol %, respectively, where 0 and 100 vol % correspond to the two cases of pure solvent I and II. When solvent I is replaced by solvent II in sequence, the PTN-3 assemblies transform from hexagonal cylinders (HC_t) to stepped bilayer lamellae (L) and to isotropic phases (I), in reverse of the direction of morphology transition induced by decreasing the tether block ratio f_t in pure solvent I (see Figure 13a1−c1). In other words, the above phase transition in mixed solvent also can be induced along the f_t increasing
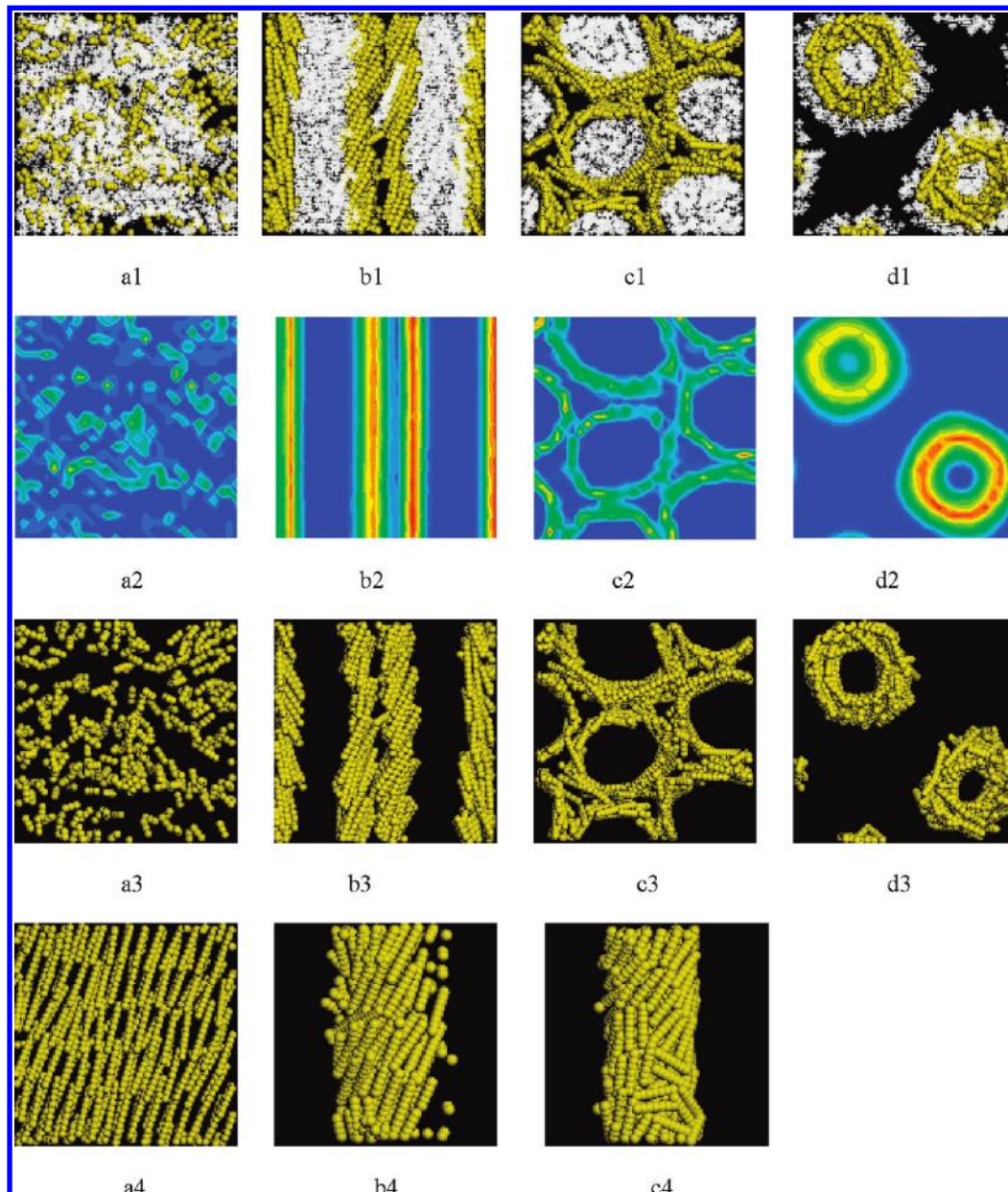
Figure 13. Simulation snapshots and rod concentration profiles obtained from systems of PTN-3. In the rod-selective solvent: $L_t = 14$ with $L_r = 3$, 9, and 11 in (a1−c1) and (a2−c2). In tether-selective solvent: $L_t = 4$ and $L_r = 7$ in (d1−d3). Tethers removed for viewing ease in (a3−d3). Corresponding to (b3−d3), the local packing of the rods in a single layer extracted from simulation is shown in (a4−c4).
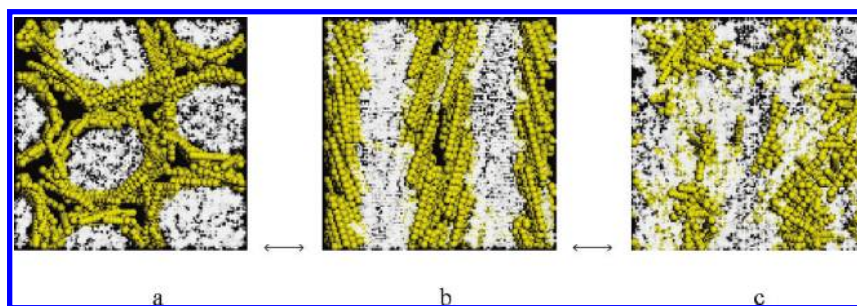

Figure 14. Morphological changes of PTN-3 in the I/II mixed solvent with the II contents of (a) 0 vol %, (b) 30 vol %, and (c) 100 vol %. Here, $L_r = 11$ and $L_t = 14$.

direction in pure solvent I marked out by the arrows in phase diagram (see Figure 12). Also, for PTN-3 molecules, it can be inferred that the increasing of the tether-selective solvent (solvent II) content is equivalent to enhancing the tether block ratio f_t of PTN-3 in the case of pure solvent I. Moreover, the self-

assembled structure can reversibly transform from one morphology to another by dynamically changing the solvent condition. Consequently, the similar conclusion, which has been summarized for the case of PTN-1 dissolved in the mixed I/II solvent, is also suitable for PTN-3. That is, partially varying
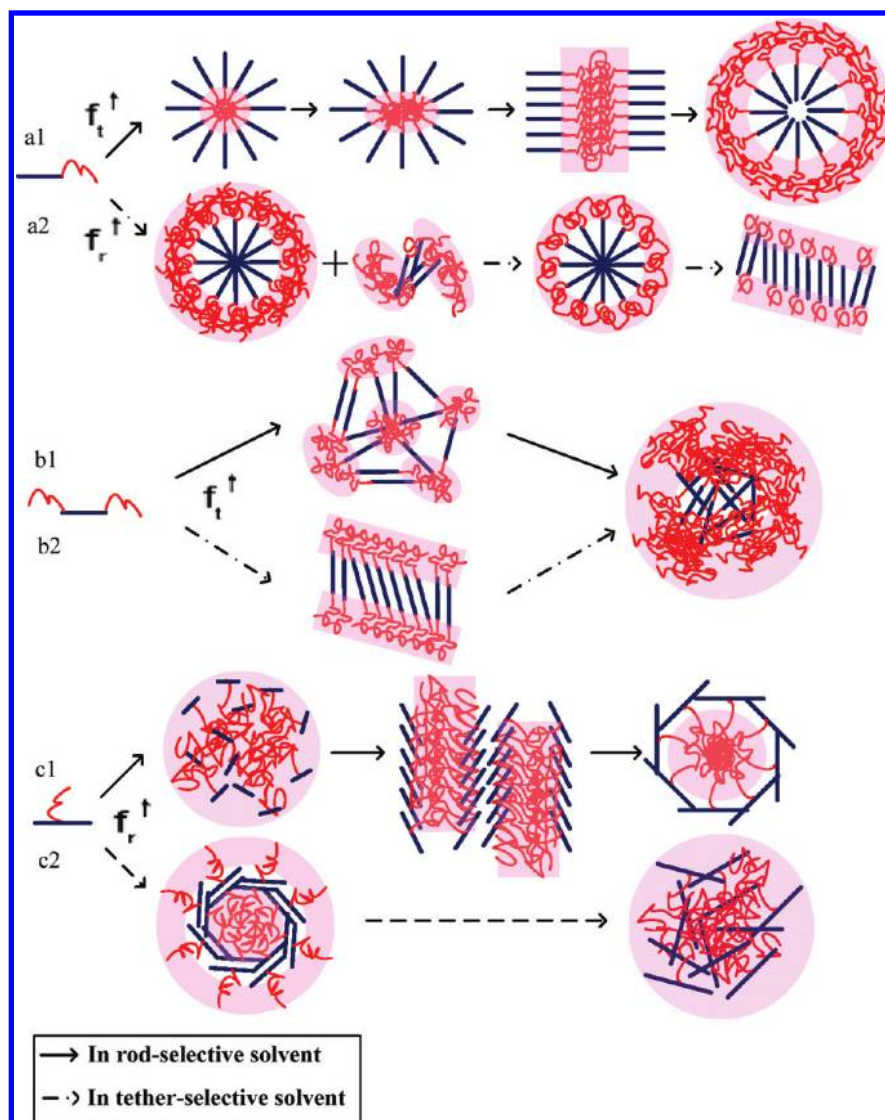
Solvent-Induced Self-Assembly of PTNs

J. Phys. Chem. B, Vol. 114, No. 21, 2010 **7199**

Figure 15. Schematic showing various morphologies upon the molecular topology, rod/tether length ratio, and solvent selectivity.

solvent quality for the block in the mixed solvent can induce a series of morphologies and reversible morphological transitions, which is equivalent to change the corresponding block ratio in pure solvent. Nguyen et al. also demonstrated that a helical morphology could be spontaneously switched from one structure to another when the solvent condition was changed.[42]

Figure 15 schematically shows the induced morphology transition process for the three types of PTN molecules in selective solvent. For PTN-1 dissolved in rod-selective solvent (panel a1), as the increase of tether length L_t, i.e., the increase of f_t, and the swelling of the inner tether core, it leads to an increase of interfacial tension. To minimize total surface energies and relax flexible chain stretching, the system must seek an efficient morphology, so its aggregates undergo the following phase transformation: tether filled cylinder (C_t) → elliptical cylinder → lamellae (L) → hollow cylinder (C_r). Oppositely in tether-selective solvent (panel a2), with the increase of rod ratio (f_r) by decreasing tether length L_t, the hydrophobic rods favor parallel packing as bundles, to minimize the interfacial energy between the rods and solvents. The self-assembly of PTN-2 in pure selective solvent (panel b1, b2) is dominated by two different processes: the association governed by tethers in rod-selective solvent and the micellization governed by rods in tether-selective solvent. Likewise, for PTN-3 with special structure from middle grafted placement (panel c1, c2), its self-assembly is determined

by the competition between maximizing the rod—rod contacts and the entropy contributed by the tethers. Briefly, for polymer-tethered nanorods in selective solvent, their assemblies depend on the competition between the stretching of tethers, liquid crystalline of rods, interfacial energy, and solvent selectivity.

4. Conclusions

We use the DPD method to examine the self-assembly of polymer-tethered nanorods (PTN) under different solvent conditions: the pure rod-selective solvent I, the pure tether-selective solvent II, and the I/II mixed solvent. The solvent-induced morphologies of PTN are much richer than that in the bulk. These morphologies depend on the topology, rod/tether length ratio, solvent selectivity, and mixed solvent content. The observed micellar structures include: cylinders, hexagonal cylinders, bilayer lamellae, lamellae/cylinder mixed phases, inverted hollow cylinders, nematic bundles, and ordered LC phases. Finally, we conclude that for pure selective solvent the morphologies and morphological transitions of PTN assemblies are affected by the rod/tether length ratio. For the mixed solvent with inverse selectivity, the similar morphologies and reversible morphological transitions for the pure solvent case can also be equivalently induced by varying mixed solvent content in sequence. These self-assembled structures are formed by the

competition between the stretching of tethers, liquid crystalline of rods, interfacial energy, and solvent selectivity.

References and Notes

(1) Zhang, X.; Chan, E. R.; Glotzer, S. C. *J. Chem. Phys.* **2005**, *123*, 184718.

(2) Iacovella, C. R.; Horsch, M. A.; Zhang, Z.; Glotzer, S. C. *Langmuir* **2005**, *21*, 9488.

(3) Chan, E. R.; Zhang, X.; Lee, C. Y.; Neurock, M.; Glotzer, S. C. *Macromolecules* **2005**, *38*, 6168.

(4) Zhang, Z. L.; Glotzer, S. C. *Nano Lett.* **2004**, *4*, 1407.

(5) Zhang, Z. L.; Horsch, M. A.; Lamm, M. H.; Glotzer, S. C. *Nano Lett.* **2003**, *3*, 1341.

(6) Bates, M. A.; Walker, M. *Phys. Chem. Chem. Phys.* **2009**, *11*, 1893.

(7) Cheung, D. L.; Troisi, A. *Phys. Chem. Chem. Phys.* **2009**, *11*, 2105.

(8) Murray, C. B.; Kagan, C. R.; Bawendi, M. G. *Annu. Rev. Mater. Sci.* **2000**, *30*, 545.

(9) Busbee, B. D.; Obare, S. O.; Murphy, C. J. *Adv. Mater.* **2003**, *15*, 414.

(10) Sun, Y. G.; Xia, Y. N. *Science* **2002**, *298*, 2176.

(11) Pinna, N.; Weiss, K.; Urban, J.; Pileni, M. P. *Adv. Mater.* **2001**, *13*, 261.

(12) Jin, R. C.; Cao, Y. W.; Mirkin, C. A.; Kelly, K. L.; Schatz, G. C.; Zheng, J. G. *Science* **2001**, *294*, 1901.

(13) Park, S.; Lim, J. H.; Chung, S. W.; Mirkin, C. A. *Science* **2004**, *303*, 348.

(14) Li, C. P.; Yeh, S. W.; Chang, H. C.; Huang, J. Y.; Wei, K. H. *Small* **2006**, *2*, 359.

(15) Harnack, O.; Pacholski, C.; Weller, H; Yasuda, A.; Wessels, J. M. *Nano Lett.* **2003**, *3*, 1097.

(16) Li, L. S.; Alivisatos, A. P. *Adv. Mater.* **2003**, *15*, 408.

(17) Duan, X. F.; Huang, Y.; Agarwal, R.; Lieber, C. M. *Nature* **2003**, *421*, 241.

(18) Crane, A. J.; Martınez-Veracoechea, F. J.; Escobedob, F. A.; Müller, E. A. *Soft Matter* **2008**, *4*, 1820.

(19) Wilson, M. R.; Thomas, A. B.; Dennison, M.; Masters, A. J. *Soft Matter* **2009**, *5*, 363.

(20) Chen, J. Z.; Zhang, C. X.; Sun, Z. Y.; An, L. J.; Tong, Z. J. *J. Chem. Phys.* **2007**, *127*, 024105.

(21) Klok, H. A.; Lecommandoux, S. *Adv. Mater.* **2001**, *13*, 1217.

(22) Lee, M.; Cho, B. K.; Zin, W. C. *Chem. Rev.* **2001**, *101*, 3869.

(23) Wang, H. B.; Wang, H. H.; Urban, V. S.; Littrell, K. C.; Thiyagarajan, P.; Yu, L. P. *J. Am. Chem. Soc.* **2000**, *122*, 6855.

(24) Li, K.; Wang, Q. *Macromolecules* **2004**, *37*, 1172.

(25) Ryu, J. H.; Oh, N. K.; Zin, W. C.; Lee, M. *J. Am. Chem. Soc.* **2004**, *126*, 3551.

(26) Long, Y. J.; Bae, J. Y.; Ryu, J. H.; Lee, M. *Angew. Chem., Int. Ed.* **2006**, *45*, 650.

(27) Hong, D. J.; Lee, E.; Jeong, H.; Lee, J.; Zin, W. C.; Nguyen, T. D.; Glotzer, S. C.; Lee, M. *Angew. Chem., Int. Ed.* **2009**, *48*, 1664.

(28) Chen, J. Z.; Zhang, C. X. *J. Chem. Phys.* **2006**, *124*, 104907.

(29) Chen, J. Z.; Sun, Z. Y.; Zhang, C. X.; An, L. J.; Tong, Z. *J. Chem. Phys.* **2008**, *128*, 074904.

(30) Tschierske, C. *Chem. Soc. Rev.* **2007**, *36*, 1930.

(31) Lintuvuori, J. S.; Wilson, M. R. *Phys. Chem. Chem. Phys.* **2009**, *11*, 2116.

(32) Song, J. H.; Shi, T. F.; Li, Y. Q.; Chen, J. Z.; An, L. J. *J. Chem. Phys.* **2008**, *129*, 054906.

(33) Loos, K.; Bo1ker, A.; Zettl, H.; Zhang, M. F.; Krausch, G.; Muller, A. H. E. *Macromolecules* **2005**, *38*, 873.

(34) Koh, H. D.; Par, J. W.; Rahman, M. S.; Changez, M.; Lee, J. S. *Chem. Commun.* **2009**, 4824.

(35) Olsen, B. D.; Segalman, R. A. *Mater. Sci. Eng., R* **2008**, *62*, 37.

(36) Cuendias, A. D.; Hellaye, M. L.; Lecommandoux, S.; Cloutet, E.; Cramail, H. J. *Mater. Chem.* **2005**, *15*, 3264.

(37) Park, J. W.; Thomas, E. L. *Macromolecules* **2004**, *37*, 3532.

(38) Lin, J. P.; Lin, S. L.; Zhang, L. S.; Nose, T. *J. Chem. Phys.* **2009**, *130*, 094907.

(39) Horsch, M. A.; Zhang, Z. L.; Glotzer, S. C. *Phys. Rev. Lett.* **2005**, *95*, 056105.

(40) Horsch, M. A.; Zhang, Z. L.; Glotzer, S. C. *J. Chem. Phys.* **2006**, *125*, 184903.

(41) Horsch, M. A.; Zhang, Z. L.; Glotzer, S. C. *Nano Lett.* **2006**, *6*, 2406.

(42) Nguyen, T. D.; Glotzer, S. C. *Small* **2009**, *5*, 2092.

(43) Wu, J.; Pearce, E. M.; Kwei, T. K. *Macromolecules* **2002**, *35*, 1791.

(44) Lin, S. L.; Numasawa, N.; Nose, T.; Lin, J. P. *Macromolecules* **2007**, *40*, 1684.

(45) Zhang, J.; Lin, W. R.; Liu, A. H.; Yu, Z. N.; Wan, X. H.; Liang, D. H.; Zhou, Q. F. *Langmuir* **2008**, *24*, 3780.

(46) Lin, W. R.; Zhang, J.; Wan, X. H.; Liang, D. H.; Zhou, Q. F. *Macromolecules* **2009**, *42*, 4090.

(47) Tung, Y. C.; Wu, W. C.; Chen, W. C. *Macromol. Rapid Commun.* **2006**, *27*, 1838.

(48) Tung, Y. C.; Chen, W. C. *React. Funct. Polym.* **2009**, *69*, 507.

(49) Lin, C. H.; Tung, Y. C.; Ruokolainen, J.; Mezzenga, R.; Chen, W. C. *Macromolecules* **2008**, *41*, 8759.

(50) Lin, S. T.; Tung, Y. C.; Chen, W. C. *J. Mater. Chem.* **2008**, *18*, 3985.

(51) Hoogerbrugge, P. J.; Koelman, J. M. V. A. *Europhys. Lett.* **1992**, *19*, 155.

(52) Groot, R. D.; Warren, P. B. *J. Chem. Phys.* **1997**, *107*, 4423.

(53) Irfachsyad, D.; Tildesley, D.; Malfreyt., P. *Phys. Chem. Chem. Phys.* **2002**, *4*, 3008.

(54) He, L. L.; Zhang, L. X.; Liang, H. J. *J. Phys. Chem. B* **2008**, *112*, 4194.

(55) He, L. L.; Zhang, L. X.; Liang, H. J. *J. Chem. Phys.* **2009**, *130*, 144907.

(56) AlSunaidi, B. A.; den Otter, W. K.; Clarke, J. H. R. *Phil. Trans. R. Soc. London* **2004**, *362*, 1773.

(57) Irving, J. H.; Kirkwood, J. G. *J. Chem. Phys.* **1950**, *18*, 817.

(58) Goujon, F.; Malfreyt, P.; Tildesley, D. J. *Macromolecules* **2009**, *42*, 4310.

(59) Widom, B. *J. Chem. Phys.* **1963**, *39*, 2808.

(60) Powles, J. G.; Holtz, B.; Evans, W. A. B. *J. Chem. Phys.* **1994**, *101*, 7804.

(61) Velázquez, M. E.; Gama-Goicochea, A.; González-Melchor, M.; Neria, M.; Alejandre, J. *J. Chem. Phys.* **2006**, *124*, 084104.

(62) Vriezema, D. M.; Hoogboom, J.; Velonia, K.; Takazawa, K.; Christianen, P. C. M.; Maan, J. C.; Rowan, A. E.; Nolte, R. J. M. *Angew. Chem., Int. Ed.* **2003**, *42*, 772.

(63) Zhou, Y. Q.; Hall, C. K.; Karplus, M. *Phys. Rev. Lett.* **1996**, *77*, 2822.